PIP aquaporin pH sensing is regulated by the length and charge of the C-terminal region

Florencia Scochera[1], Gerardo Zerbetto De Palma[1,2,3], Agustina Canessa Fortuna[1], Jonathan Chevriau[2], Roxana Toriano[4], Gabriela Soto[5,6], Ari Zeida[7] and Karina Alleva[1,2] (iD)

1 Facultad de Farmacia y Bioquímica, Departamento de Fisicomatemática, Universidad de Buenos Aires, Argentina
2 Instituto de Química y Fisicoquímica Biológica (IQUIFIB), Facultad de Farmacia y Bioquímica, CONICET, Universidad de Buenos Aires, Argentina
3 Instituto de Biotecnología, Universidad Nacional de Hurlingham, Villa Tesei, Argentina
4 Facultad de Medicina, CONICET, Instituto de Fisiología y Biofísica "Bernardo Houssay" (IFIBIO "Houssay"), Universidad de Buenos Aires, Argentina
5 Instituto de Agrobiotecnología y Biología Molecular (INTA-CONICET), Buenos Aires, Argentina
6 Instituto de Genética (INTA), Buenos Aires, Argentina
7 Departamento de Bioquímica and Centro de Investigaciones Biomédicas (Ceinbio), Facultad de Medicina, Universidad de la República, Montevideo, Uruguay

Plant PIP aquaporins play a central role in controlling plant water status. The current structural model for PIP pH-gating states that the main pH sensor is located in loopD and that all the mobile cytosolic elements participate in a complex interaction network that ensures the closed structure. However, the precise participation of the last part of the C-terminal domain (CT) in PIP pH gating remains unknown. This last part has not been resolved in PIP crystal structures and is a key difference between PIP1 and PIP2 paralogues. Here, by a combined experimental and computational approach, we provide data about the role of CT in pH gating of *Beta vulgaris* PIP. We demonstrate that the length of CT and the positive charge located among its last residues modulate the pH at which the open/closed transition occurs. We also postulate a molecular-based mechanism for the differential pH sensing in PIP homo- or heterotetramers by performing atomistic molecular dynamics simulations (MDS) on complete models of PIP tetramers. Our findings show that the last part of CT can affect the environment of loopD pH sensors in the closed state. Results presented herein contribute to the understanding of how the characteristics of CT in PIP channels play a crucial role in determining the pH at which water transport through these channels is blocked, highlighting the relevance of the differentially conserved very last residues in PIP1 and PIP2 paralogues.

Introduction

Plants depend on strict regulation of water transport for their growth and development. Aquaporins (AQP) are the channels that ensure a rapid and reversible control of water permeability. Plant aquaporins compose a large and diverse protein family whose functions are not limited to water homeostasis but are also engaged in the transport of key molecules such as CO_2, H_2O_2, NH_3, urea, ions, and micronutrients [1,2]. Higher plant AQP are organized into five subfamilies: the plasma membrane intrinsic proteins (PIPs), the tonoplast intrinsic proteins (TIPs), the nodulin 26-like intrinsic proteins (NIPs), the small basic intrinsic proteins (SIPs), and the X intrinsic proteins (XIPs). Among these channels, PIP constitutes the most numerous and homogeneous group with a central role in affecting root and leaf hydraulic properties [2]. Two main features distinguish PIP from other AQP: the possibility of assembling as heterotetramers combining different isoforms from the two groups of paralogues—PIP1 and PIP2—[3] and the gating mechanism mediated by its unusually long intracellular loopD [4–6]

The known characteristics for modern PIP1 and PIP2 isoforms in terms of their water transport activity, trafficking, and heterotetramerization emerged early in the evolution of vascular plants [7].

Interestingly, even with the huge number of PIP isoforms per genome and the splitting into two groups of paralogues, there is a high sequence identity among all PIP across species in comparison with other plant AQP subfamilies, suggesting a great evolutionary constraint [8,9]. Among PIP1 and PIP2 channels, there is more than 80% of sequence identity. The main differences between both paralogues' sequences are in the length of their terminal domains. PIP2 C-terminal region (CT) is around 18 to 23 residues long, while PIP1 CT is approximately 6 to 8 residues shorter (Fig. 1A,B). On the contrary, PIP1 N-terminal region (NT) is longer than PIP2 NT. The interaction between PIP1 and PIP2 within heterotetramers has been reported to occur throughout different plant species, and variable stoichiometry has been described for strawberry, red beet, and maize PIP [10–12]. Many reports show that the biophysical properties of PIP1 and PIP2 channels depend on the kind of tetramers—homo- or heterotetramer—of which they are part 10,11,13–15. Intracellular pH, together with changes in calcium concentration, is a signal that triggers the gating of PIP channels [4,16,17]. Conditions such as anoxia or hypoxia have been linked to plant cell cytosolic acidification and to the consequent reduction in hydraulic conductivity by PIP channel closure [4]. A mechanistic model for PIP gating was proposed
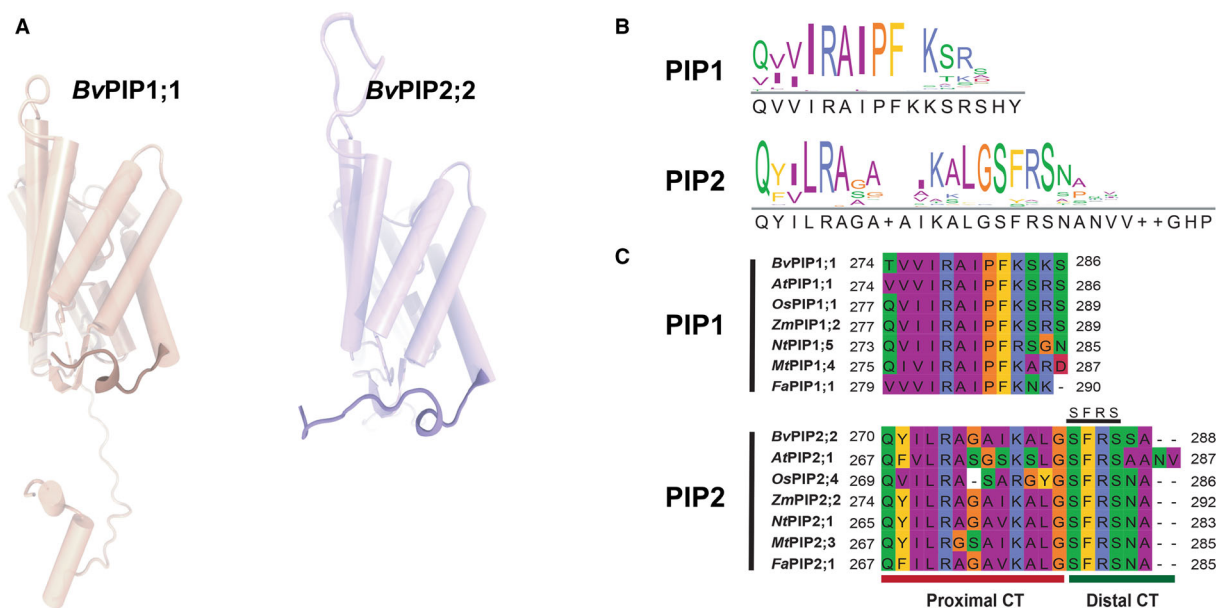
Fig. 1. PIP2 and PIP1 C-terminal sequences and structure. (A) *Bv*PIP1;1 and *Bv*PIP2;2 homology models. CT is represented in dark orange and dark purple, respectively. Model renders were obtained with VMD software. (B) Logo of PIP1 and PIP2 CT sequences showing the degree of conservation of each residue. (C) Multiple sequence alignment of selected PIP1 and PIP2 CT showing proximal (underlined in red) and distal parts (underlined in green) and the PIP2 SFRS motif (underlined in black).

after obtaining *So*PIP2;1 high-resolution structures in both open and closed conformations [5,6]. This model proposes that the principal pH sensor is a histidine residue located in loopD and that the open/closed transition involves a conformational change in cytosolic loopD that alters the position of a leucine residue inside the water pore. This leucine was shown to be the key blocking residue in the closed state of PIP channels [6,18]. Contacts among loopD, loopB, and NT were proposed to stabilize the closed state. It was also proposed that CT serine residues are involved in this network [19]; however, controversy persists since it was shown that, in the case of *Nt*PIP2;1 pH gating, CT serines are not involved [20].

So far, among PIP, only homotetrameric PIP2 structures have been determined by X-ray crystallography [6,21]. Although there is no structural information for PIP1 channels, the high similarity of their transmembrane helices and loopD with those of PIP2 and experimental evidence showing that some PIP1 can be also inhibited by acidification [4], allow speculating that a conserved mechanism for the conformational change is present in both paralogues. However, a shifted $pH_{0.5}$ in the open/close transition has been found for PIP1-PIP2 heterotetramers in comparison with PIP2 homotetramers [22]. Considering that CT length is one of the main structural differences among PIP1 and PIP2, we wonder in which way CT could participate in this differential pH regulation.

*Bv*PIP2;2 is a pH-gated aquaporin from red beet *Beta vulgaris* whose biophysical characterization under different pH conditions is available from previous studies both for homo- and heterotetramers with *Bv*PIP1;1 [11,18,22,23]. So, we consider *Beta vulgaris* PIP channels as suitable candidates to investigate the role of the CT in PIP pH gating.

In the present study, we combine *in vitro* experiments with MDS of PIP models, which include mobile terminal ends to demonstrate that the last residues of PIP sequences, differentially conserved in PIP1 and PIP2 paralogues, play a role in determining the pH at which can occur the open/closed transition of these channels.

Results

Truncation of the *Bv*PIP2;2 CT induced an alkaline shift on the pH dose–response curve

PIP1 and PIP2 channels are plant paralogues with highly conserved sequences whose cytosolic CT present different lengths (Fig. 1). Considering the structural information available for PIP2 channels, PIP2 CT can be divided into two sections: the proximal section, ordered (solved in crystal structures), and a distal section with high mobility and putative disorder (not solved in crystal structures) (Fig. 1C). The distal section contains a very conserved short linear SFRS motif and a variable part whose length and sequence depend on the isoform (Fig. 1C). This section is absent in PIP1 channels.

To evaluate whether this last part of the protein sequence participates in pH gating, we constructed a *Bv*PIP2;2 mutant with a shorter CT, *Bv*PIP2;2Δ6CT. The deletion involved the last 6 residues of the sequence, SFRSSA, so the CT of the truncated channel lacks its putative most flexible part and is as long as any PIP1 CT. Injection of *Bv*PIP2;2Δ6CT cRNA into *Xenopus laevis* oocytes leads to an increase in the osmotic water permeability coefficient (P_f), indicating that the truncated channels are properly expressed, form tetramers that locate in the plasma membrane, and are permeable to water. We then analyzed pH sensing for *Bv*PIP2;2Δ6CT and found a shift to alkaline values in the P_f *vs* pH dose–response curves when compared with the typical behavior of wild-type *Bv*PIP2;2 (Fig. 2A,B). The $pH_{0.5}$ corresponding to the response of *Bv*PIP2;2Δ6CT and *Bv*PIP2;2 is 6.80 ± 0.07 (mean $\pm$ SEM, $n = 3$) and 6.45 ± 0.02 (mean $\pm$ SEM, $n = 4$), respectively (Fig. 2C). These results confirm that the very last 6 residues of *Bv*PIP2;2 are not essential for transport activity but are clearly involved in pH sensing.

We also analyzed a truncated mutant of an alternative PIP2 channel (*Medicago truncatula* PIP2;3) whose last residues are SFRSNA, and results obtained are similar to those obtained for *Bv*PIP2;2Δ6CT, 6.97 ± 0.01 for *Mt*PIP2;3Δ6CT *vs* 6.51 ± 0.02 for *Mt*PIP2;3 (mean $pH_{0.5} \pm$ SEM, $n = 2$).

Mutation S283A does not affect *Bv*PIP2;2 pH dose–response curve while mutation R285A induces an alkaline shift

To clarify the cause in $pH_{0.5}$ shifting of PIP2 with short CT, we analyzed if this happens as a result of the particular action of one residue of the highly mobile end of the protein. Two residues were of particular interest, S283 and R285. So, we mutated each of these to alanine and analyzed the impact of these mutations in pH dose–response curves. As can be seen in Fig. 3, *Bv*PIP2;2S83A forms functional channels, that is, transports water and is sensitive to pH. The dose–response curve for this mutant channel is similar to the one obtained for the wild-type *Bv*PIP2;2, indicating that S283 is not involved in pH gating (6.49 ± 0.01, mean $pH_{0.5} \pm$ SEM, $n = 3$). This result
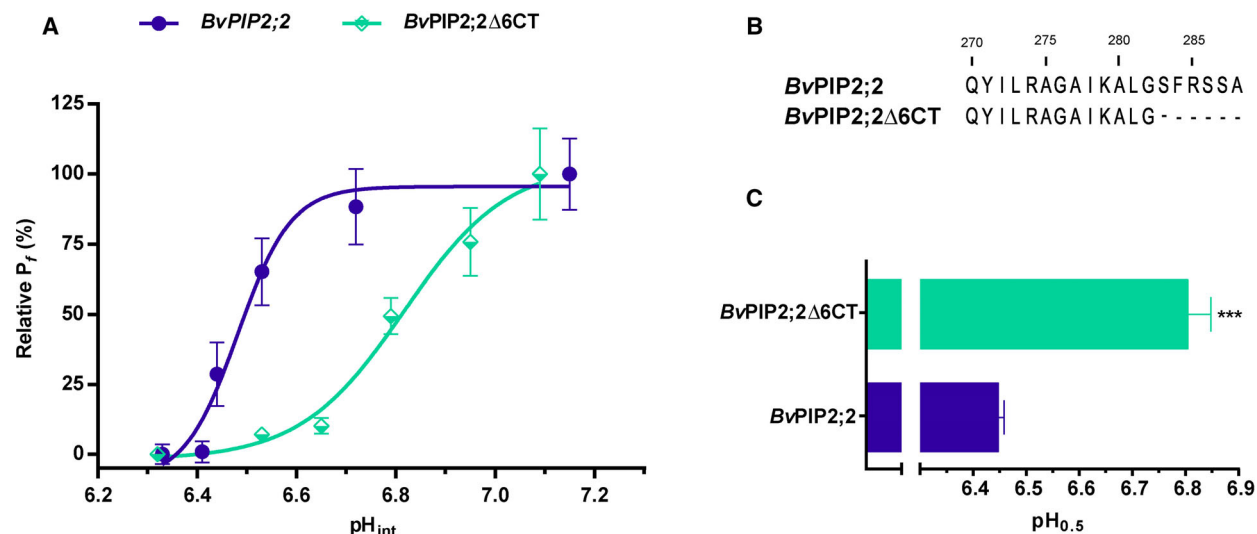
Fig. 2. pH dose–response curve of normalized water permeability (P$_f$) of oocytes expressing *Bv*PIP2;2 in comparison with oocytes expressing the truncated channel *Bv*PIP2;2Δ6CT. (A) Relative P$_f$ behavior after cytosolic acidification was tested on oocytes injected with cRNA coding for *Bv*PIP2;2 or *Bv*PIP2;2Δ6CT. Data points are values obtained using 8–16 oocytes for each pH$_{int}$ from a same batch in a representative experiment. (B) Wild-type and truncated CT sequences are shown. (C) The pH$_{0.5}$ values are reported as the average of three to four independent experiments (mean pH$_{0.5}$ ± SEM). An unpaired *t*-test was used to test the statistical difference between treatments (***, $P < 0.001$).
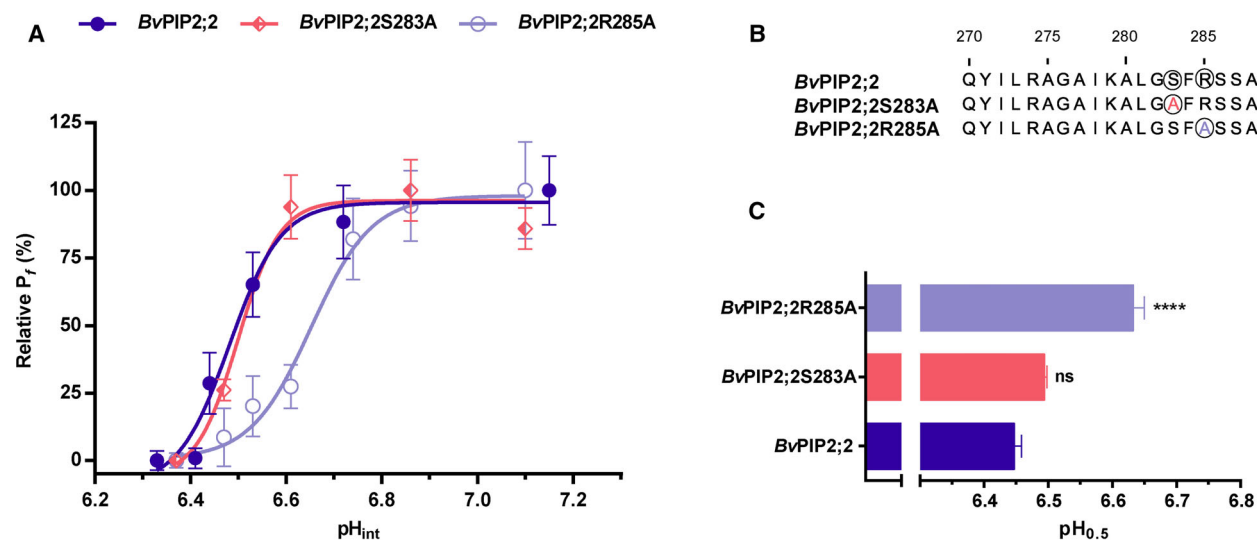

Fig. 3. pH dose–response curve of relative membrane water permeability (P$_f$) of oocytes expressing *Bv*PIP2;2S283A or *Bv*PIP2;2R285A. (A) P$_f$ behavior after cytosolic acidification was tested on oocytes injected with cRNA coding for *Bv*PIP2;2S283A or *Bv*PIP2;2R285A in comparison with the behavior of P$_f$ of oocytes expressing *Bv*PIP2;2. Data points are values obtained from the same batch of oocytes (8–13 oocytes were used for each pH$_{int}$). The curves shown are representative of three independent experiments using different oocyte batches. (B) Sequences of *Bv*PIP2;2 and mutants are shown indicating with circles the mutated residues. (C) The pH$_{0.5}$ values are reported as the average of three independent experiments (pH$_{0.5}$ ± SEM). Dunnett multiple comparison test was used to calculate the statistical difference between the wild-type and the two mutants (****, $P < 0.0001$; ns, not significant).

is in agreement with the previous report on *Nt*PIP2;1 Ser277, where the mutant *Nt*PIP2;1S277A was shown to be effectively blocked by acidification [20].

The other conserved residue we explored among the last 6 of *Bv*PIP2;2 CT as potentially involved in the control of the pH$_{0.5}$ was the basic residue R285.

*Bv*PIP2;2R285A forms functional channels, that is, transports water and is sensitive to pH (Fig. 3). Interestingly, the P_f *vs* pH dose–response curve for this mutant shifts to the right in comparison with the wild-type *Bv*PIP2;2 curve, indicating that the R285 is a key residue in PIP2 pH gating (6.63 ± 0.02, mean $pH_{0.5} \pm$ SEM, $n = 3$). The rightward pH shifting found for *Bv*PIP2;2R285A (~ 0.18 pH units) was not of the same magnitude as the one registered for *Bv*PIP2;2Δ6CT (~ 0.35 pH units). This discrepancy proves that R285 is a relevant residue in pH gating but not a unique factor.

PIP1 CT alters PIP channels open/closed transition at $pH_{0.5}$ in a similar way to short PIP2 CT

Since *Bv*PIP1;1 presents a shorter CT than *Bv*PIP2;2, we investigated if *Bv*PIP1;1 CT could elicit a response similar to truncated PIP CT in pH gating. We replaced the *Bv*PIP2;2 CT by *Bv*PIP1;1 CT to create a chimeric protein, *Bv*PIP2;2CT1;1. The CT of this chimeric protein is as short as in *Bv*PIP2;2Δ6CT but with a different sequence (Fig. 4A,B). The injection of *Bv*PIP2;2CT1;1 cRNA in *Xenopus laevis* oocytes did not provoke the increase in P_f values expected for a functional water channel at any of the tested cRNA

quantities, but it did when co-expressed with *Bv*PIP2;2 or *Bv*PIP1;1. This behavior could be due to a difficulty of *Bv*PIP2;2CT1;1 homotetramers to be located at plasma membrane while conserving the ability to interact with other PIP channels to form heterotetramers. When pH response of the co-expression of *Bv*PIP2;2CT1;1 with *Bv*PIP1;1 was assayed, the open/closed transition presented a $pH_{0.5}$ of 6.82 ± 0.05 (mean $pH_{0.5} \pm$ SEM, $n = 3$) (Fig. 4C) resembling the values obtained for any stoichiometric ensemble of *Bv*PIP2;2 with *Bv*PIP1;1. However, contrasting with those heterotetrameric channels, where two different kinds of CT are present, "PIP2 type" and "PIP1 type", here the four CTs are short and "PIP1 type." So, we tested the co-expression of *Bv*PIP2;2CT1;1 with *Bv*PIP2;2. This ensemble showed a rightward shifting of the pH response in comparison with *Bv*PIP2;2 homotetramers, but to a lesser extent of the reported for any stoichiometric ensemble of *Bv*PIP2;2 and *Bv*PIP1;1 (6.64 ± 0.02, mean $pH_{0.5} \pm$ SEM, $n = 3$) (Fig. 4). Now, two different kinds of CT are present, "PIP2 type" and "PIP1 type," but unlike in the case of *Bv*PIP2;2-*Bv*PIP1;1 co-expression where not only the CT is different but also the NT, in this situation NT are all "PIP2 type." We comment on the possible involvement of NT in CT behavior in the next sections.
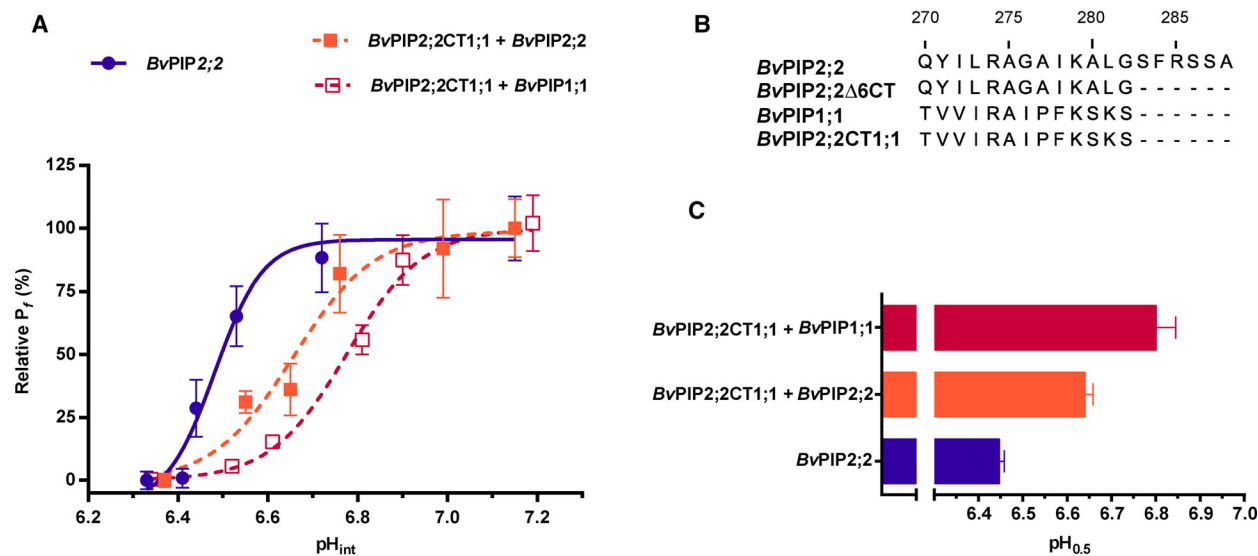

Fig. 4. P_f dependence on pH for the co-expression of *Bv*PIP2;2CT1;1 with *Bv*PIP2;2 or *Bv*PIP1;1. (A) pH dose–response curve of relative P_f of oocytes co-expressing *Bv*PIP2;2CT1;1 plus *Bv*PIP2;2 or *Bv*PIP1;1 (3 : 1 part of each cRNA per oocyte) or expressing *Bv*PIP2;2 alone. Data points are values obtained from the same batch of oocytes; 8–15 oocytes were used for each pH_{int}. The curves shown are representative of three to four independent experiments using different oocyte batches. (B) *Bv*PIP2;2, *Bv*PIP1;1, *Bv*PIP2;2Δ6CT, and *Bv*PIP2;2CT1;1 CT sequences are shown. (C) The $pH_{0.5}$ values are reported as the average of three to four independent experiments (mean $pH_{0.5} \pm$ SEM). Dunnett multiple comparison test was used to calculate the statistical difference between the wild-type and the two co-expressions (****, $P < 0.0001$; **, $P < 0.01$).

Short and long CTs can differentially affect the environment of pH sensing residues

As all the *in vitro* results presented in previous sections point to PIP2 distal CT contributing to pH sensing, we studied the behavior of long and short CTs employing MD simulations. We explored different conformations of these flexible regions, to obtain mechanistic information about possible interactions between CT and other protein residues that may help in the interpretation of the observed behavior in gating experiments. In previous work, we validated a homology model for *Bv*PIP2;2 using the structure of closed *So*PIP2;1 (PDB 1Z98) [18] as template. This model was incomplete since, as previously explained, experimentally determined PIP structures do not completely characterize NT and CT due to their intrinsic high mobility. Here, we generated a complete model of each monomer and sampled the conformational space of the whole tetrameric channel by modeling terminal domains as explained in the Materials and methods section. After obtaining a model for the whole *Bv*PIP2;2, we truncated, *in silico*, the last 6 residues of each CT to create a model of *Bv*PIP2;2Δ6CT. Finally, we performed four MD replicas of 100 ns each (400 ns total) for the complete and truncated homotetrameric channel models. Fig. 5 A depicts the conformational space sampled by CTs and loopDs in closed *Bv*PIP2;2 and *Bv*PIP2;2Δ6CT homotetramers. While in the case of *Bv*PIP2;2Δ6CT, the four short CTs accommodate between monomers and no close contacts with loopD of adjacent monomers can be visualized, interactions between long CTs and their adjacent loopDs were present in *Bv*PIP2;2. To estimate the structure flexibility of the three cytoplasmatic elements, that is, NT, CT, and loopD, both in *Bv*PIP2;2 and in *Bv*PIP2;2Δ6CT, we calculated local root-mean-square deviation (RMSD) along the simulations, as an indicator of mobile region flexibilities. Results displayed in Fig. 5B show that CTs and NTs present high, and variable among chains, RMSD values in comparison with loopDs for both systems. To better describe the interactions of loopDs with adjacent domains, we calculated the radial distribution function (RDF) of CT atoms centered in H202 (pH sensor). We found that in *Bv*PIP2;2 model, the H202 located in chain A presented a higher density of contacts at lower radial distances than H202 of the other chains (Fig. 5C). No similar behavior for a H202 in *Bv*PIP2;2Δ6CT model was detected for any of their four chains. This particular behavior of H202$_{chainA}$ makes this monomer (and its adjacent neighbor CT) an attractive model to study possible

molecular explanations for the experimental results discussed in previous sections.

Hence, we surveyed the microenvironment characteristics of chain A pH sensor (H202$_{chainA}$) in *Bv*PIP2;2 and *Bv*PIP2;2Δ6CT systems. Interestingly, in the case of *Bv*PIP2;2, H202$_{chainA}$ interacts with residues of the distal part of the CT of an adjacent monomer (chain D); these interactions are absent in *Bv*PIP2;2Δ6CT model. Fig. 6A shows representative snapshots where the area of interest and contacts above mentioned are illustrated.

In particular, H202$_{chainA}$ presents contacts with residues R285, S286, S287, and A288 of chain D. These contacts are not significantly modified with the protonation state of H202 (Fig. 6B). In the case of *Bv*PIP2;2Δ6CT, only minor interactions among H202$_{chainA}$ with residues of the proximal CT are found. Accordingly, solvent accessible surface area (SASA) values along the simulation show that H202$_{chainA}$ in *Bv*PIP2;2 is much less solvent accessible than in *Bv*PIP2;2Δ6CT (Fig. 6C).

Analyzing together the data obtained from homotetramer trajectories, it emerges that the last portion of long CT may access conformations in which loopD is affected. This kind of loopD-CT interaction was less likely for the truncated system. To test whether long CT contacts can alter H202$_{chainA}$ pKa (CT of chain D affecting loopD of chain A), we performed titration curves for this residue by means of continuous constant pH molecular dynamics (CpHMD), both for *Bv*PIP2;2 and for *Bv*PIP2;2Δ6CT. The calculated pKa values for H202$_{chainA}$ of *Bv*PIP2;2 and *Bv*PIP2;2Δ6CT were 4.96 ± 0.72 (mean $\pm$ SEM, $n = 9$) and 7.12 ± 0.51 (mean $\pm$ SEM, $n = 5$), respectively (Fig. 6 D). This shift toward alkaline values reflects the experimental tendency reported in the *in vitro* experiments. Clearly, the last 6 residues of one monomeric chain can reach the loopD pH sensor of its neighbor chain and establish crucial contacts that affect its environment. Probably, the last residues of long CT could act as a shield (steric and maybe also electrostatic) on H202 causing its pKa modification.

Environment of pH sensing residues is also affected in heterotetrameric models

In previous work, it was shown that co-expression of *Bv*PIP2;2 with *Bv*PIP1;1 produces a rightward shift of the pH response curve for water transport, altering the pH$_{0.5}$ from approximately 6.45 for the case of the expression of *Bv*PIP2;2 alone, to 6.80 for the *Bv*PIP2;2-*Bv*PIP1;1 co-expression [11,22]. We wondered if this pH$_{0.5}$ shifting could have been the
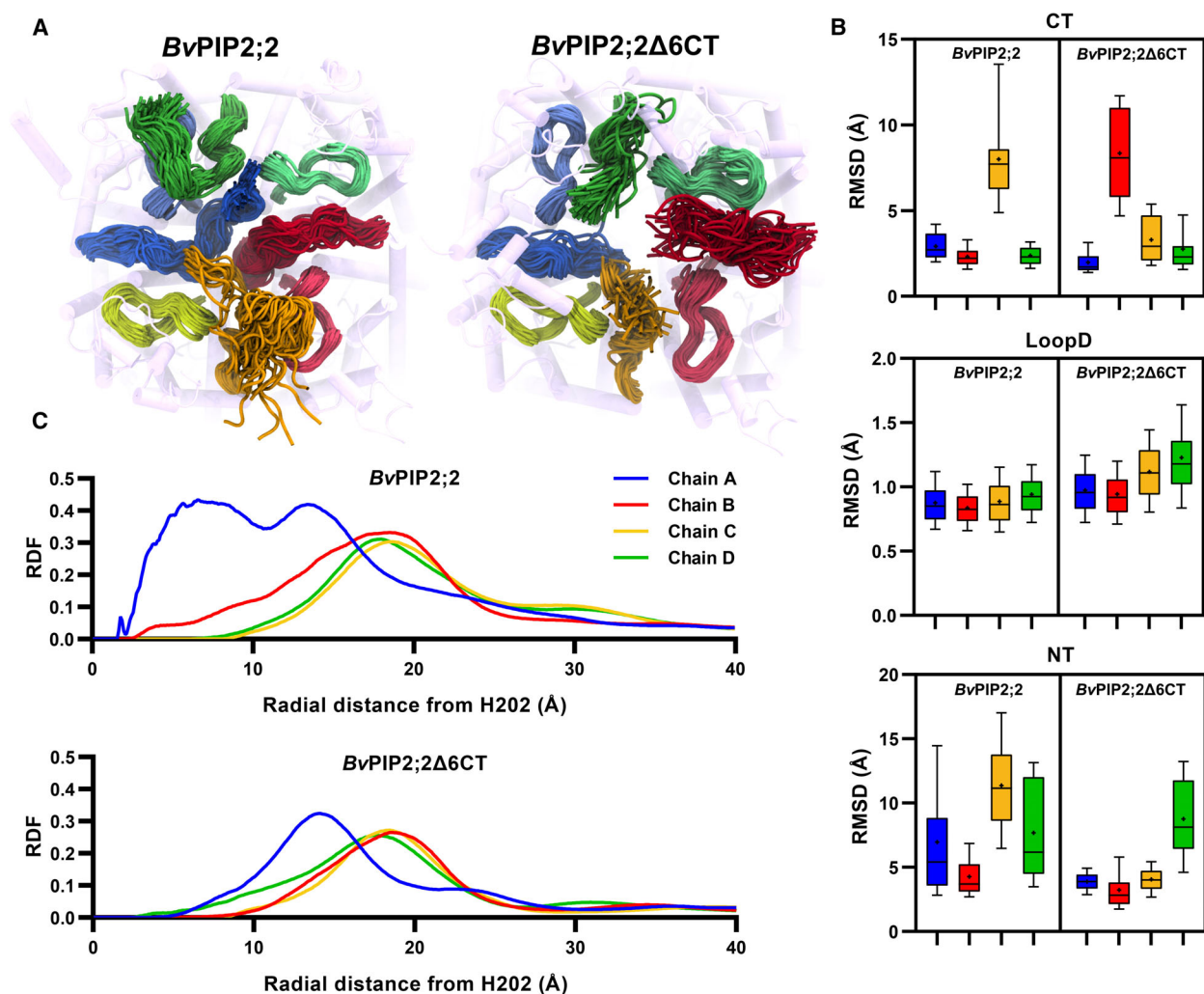
Fig. 5. Conformational sampling of intracellular flexible regions in PIP tetramers. (A) Intracellular view of *Bv*PIP2;2, *Bv*PIP2;2Δ6CT homotetramers showing CTs and loopDs in a multiframe representation. For each monomeric CT, chain is color coded: A blue, B red, C yellow, D green. Monomeric loopD has a lighter version of the corresponding chain color. Model renders were obtained with VMD software. (B) RSMD plots for CTs, loopDs, and NTs of *Bv*PIP2;2 and *Bv*PIP2;2Δ6CT. Bar colors indicate the corresponding chain as in (A). (C) Radial distribution function of CT atoms computed for each H202, accounting for CT atoms presence probability density around each pH sensor. Atoms from every CT were considered when calculating RDF for each H202. RDF curves corresponding to each H202 are color coded as in (A).

consequence of pH sensors not being shielded by CT as shown above. We prepared a heterotetrameric model of *Bv*PIP1;1 and *Bv*PIP2;2 in a 3:1 stoichiometry, with 3 molecules of *Bv*PIP1;1 and 1 of *Bv*PIP2;2, that is, 3 short CT or "PIP1 type" and 1 long CT or "PIP2 type." The PIP1 complete models were constructed following a similar procedure to PIP2. From the four kinds of available PIP2 models, we decided to use the one with the conformation where contacts among CT and loopD were detected. Conformational sampling of *Bv*PIP1;1 and *Bv*PIP2;2 CT in the 3:1 heterotetramer is shown in Fig. 7A. RDF profile for

the four chains shows clearly that all H205 (equivalent to PIP2 H202) have lower contact density at less than 10 Å in comparison with H202$_{chainA}$ in the *Bv*PIP2;2 homotetramer, including H205$_{chainA}$ that is next to the *Bv*PIP2;2 long CT in the bent conformation (Fig. 7B). Accordingly with this lack of contacts between adjacent *Bv*PIP1;1 loopD and *Bv*PIP2;2 CT, the calculated pKa value for H205$_{chainA}$ was 7.31 ± 0.47 (mean $\pm$ SEM, $n = 4$) (Fig. 7C). Again, the shift toward alkaline values detected here is in accordance with all previous experimental tendencies of pH dose–response curves of PIP2-PIP1 heterotetramers [10,11,22]. It is
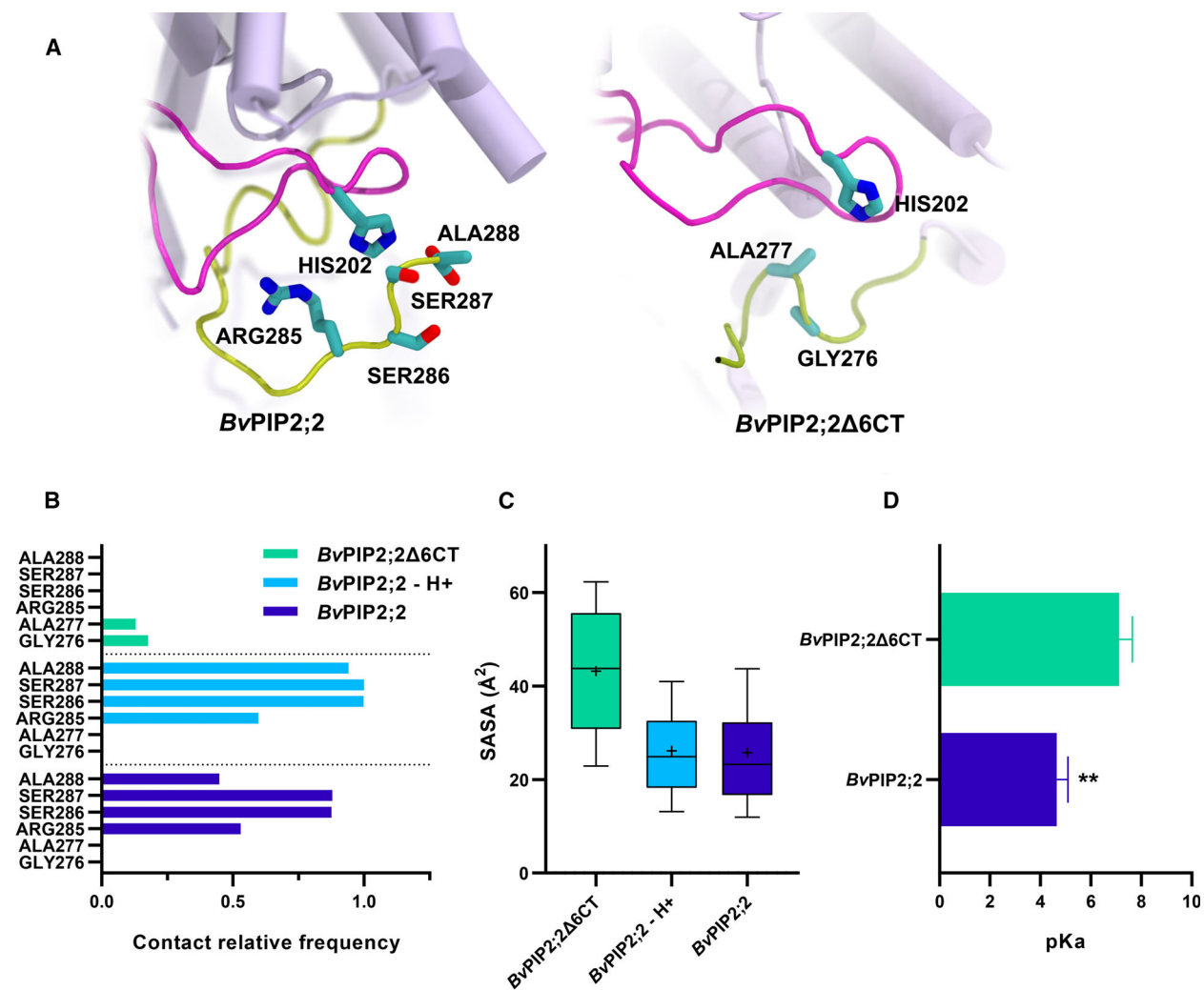
Fig. 6. Interaction of loopD H202 and CT. (A) Snapshot from *Bv*PIP2;2 and *Bv*PIP2;2Δ6CT simulations showing main contacts among loopD$_{chainA}$ (in magenta) and CT$_{chainD}$ (in green). The side chains of the H202 and contacting residues are shown as sticks. Model renders were obtained with VMD software. (B) Contact relative frequencies among H202 and the last CT residues for *Bv*PIP2;2Δ6CT, *Bv*PIP2;2-H+ (H202 protonated), and *Bv*PIP2;2. (C) Solvent accessible surface area (SASA) for H202$_{chainA}$ in *Bv*PIP2;2Δ6CT, *Bv*PIP2;2-H+, and *Bv*PIP2;2. Lower and upper boundaries of the box indicate 25th and 75th percentiles, respectively, while whiskers indicate 10th and 90th percentiles. Central line indicates 50th percentile, and mean is marked with a + sign. 8000 data points obtained from each MD trajectory were considered for statistics in panels (B) and (C). (D) Calculated pKa values for H202$_{chainA}$ after titration curves by CpHMD in for *Bv*PIP2;2Δ6CT ($n = 5$) and *Bv*PIP2;2 ($n = 10$) reported as pKa ± SEM. Student's *t*-test was used to calculate the statistical difference between *Bv*PIP2;2Δ6CT and *Bv*PIP2;2 (**, $P < 0.01$).

Fig. 7. Conformational sampling of intracellular flexible regions in PIP tetramers. (A) Intracellular view of 3 : 1 *Bv*PIP1;1-*Bv*PIP2;2 showing CT and loopD multiframe representation. *Bv*PIP2;2 monomer is colored in violet while *Bv*PIP1;1 monomers are colored in light orange. For each monomeric CT, chain is color coded: A blue, B red, C yellow, D green. Monomeric loopD has a lighter version of the corresponding chain color. Model renders were obtained with VMD software. (B) Radial distribution function of CT atoms computed for each H202. Atoms from every CT were considered when calculating RDF for each H202 in the 3:1 *Bv*PIP1;1-*Bv*PIP2;2 heterotetramer. RDF curves corresponding to each H202 are color coded as in (A). RDF for *Bv*PIP2;2 H202$_{chainA}$ is shown as a black dashed line for the sake of comparison. (C) Calculated pKa values for H205$_{chainA}$ after titration curves by CpHMD in for 3:1 *Bv*PIP1;1-*Bv*PIP2;2 ($n = 4$) in comparison with *Bv*PIP2;2 ($n = 10$), reported as pKa ± SEM. Student's *t*-test was used to assess the statistical significance of the differences (**, $P < 0.01$).

*Bv*PIP2;2-*Bv*PIP1;1

A

B

C
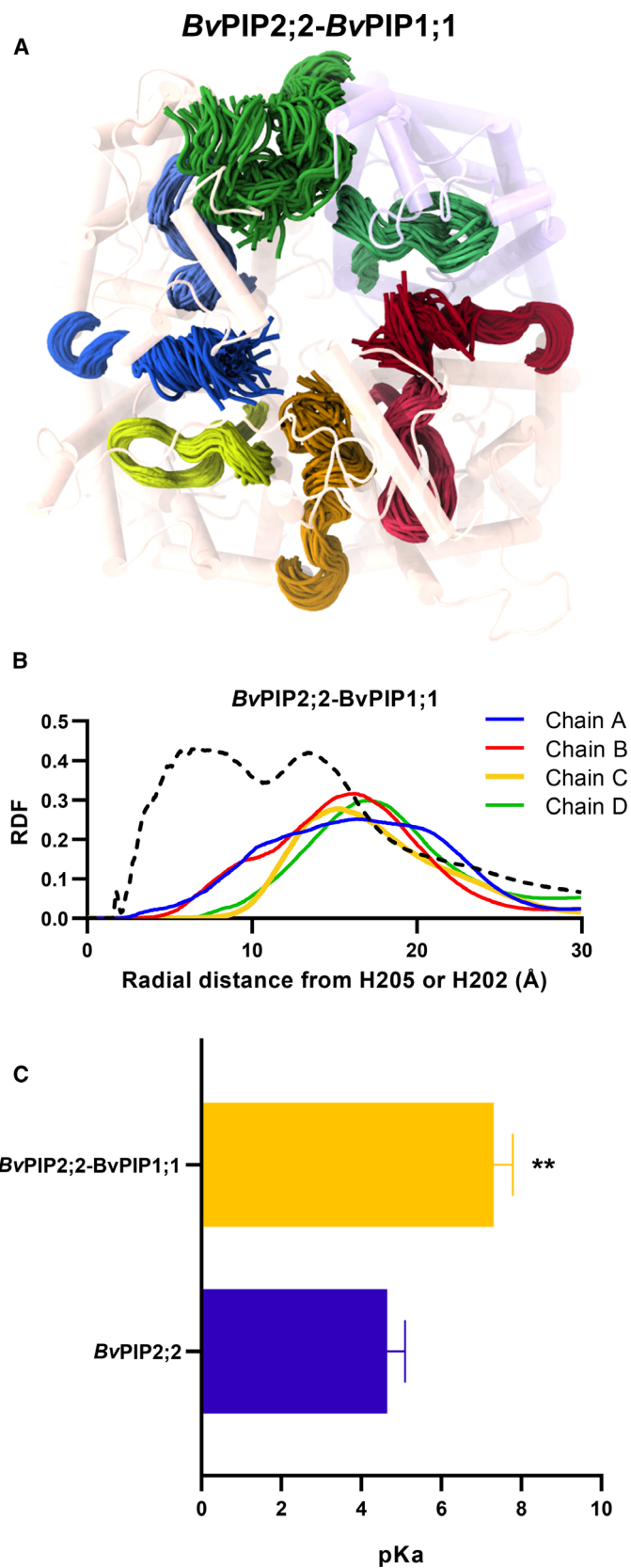
important to stress that in this case, *Bv*PIP2;2 CT is long and can reach adjacent *Bv*PIP1;1 loopD, but being part of a heterotetramer, *Bv*PIP2;2 CT distal region moves away from its adjacent loopD. This long CT behavior can be explained by the absence of other long CT nearby or by particular contacts established with *Bv*PIP1;1 NT, a region that is quite different from *Bv*PIP2;2 NT, both in sequence and in length. The detailed participation of NT in PIP pH gating goes beyond this research, and we hope it can be disclosed in future works. However, all our results taken together suggest that, only when pH sensor is interacting with a long CT, the open/close transition in PIP channels can occur at quite acidic pH values as 6.4.

Discussion

The aim of this work was to elucidate two issues pending clarification in the field of plant aquaporins: i—is PIP2 CT actually involved in pH gating? and ii—is the difference in length between PIP2 and PIP1 CT relevant for pH gating of PIP2 homo- and PIP1-PIP2 heterotetramers? Our study shed light on both questions. We demonstrate that the length of PIP2 CT and the positive charge located among its last residues are, at least, two of the factors that explain the pH at which the transition open/closed occurs. We also postulate a molecular-based mechanism for the differential pH sensing in PIP homo- or heterotetramers.

PIP2 CT is a short intracellular domain that can be divided into two sections, a proximal part and a distal part. The proximal portion is, in the closed state of the channel, ordered and positioned between adjacent monomers. Following the information provided by the open conformation of *So*PIP2;1, this proximal section moves away from its position when the channel opens, thereby allowing the movement of loopD. The distal part of CT is the structural element that, as we showed here, keeps PIP2 channels open until quite acidic cytosolic pH values are reached. The absence of this distal section (as in the truncated *Bv*PIP2;2Δ6CT) alters the pH dose–response curve approximately in 0.4 pH units. The distal CT presents the SFRS motif —highly conserved among PIP2—and extra residues that may vary depending on the isoform. The serines in SFRS motif are phosphorylation targets and have been linked to trafficking and/or water transport increase of some PIP2 channels [24,25]. A role in gating was proposed for this CT serine: when dephosphorylated, it could be part of the network of interactions that stabilize the closed state in all PIP2, and, when phosphorylated, it drives monomeric channel opening [6,19]. However, as mentioned before, the role of this

serine residue was questioned, at least as a general rule in PIP2 gating, since mutation of the equivalent S277 to alanine in *Nt*PIP2;1 did not affect the closure of this channel at pH 6 [20]. Also, the mutation of S274E in *So*PIP2;1 did not render open channels and their loopD was found to adopt the same conformation as in the wild-type closed structure [19]. Recently, the phosphorylation of CT serines in *At*PIP2;1 has been also pointed, together with another still unidentified site, as involved in the activation of the cation conductance (probably) through the central pore of PIP homotetramers [25,26]. Here, we showed that S283 in *Bv*PIP2;2, the equivalent to S274 in *So*PIP2;1, can be replaced by alanine without altering proper plasma membrane localization, water transport in the open state, or pH gating in *Xenopus laevis* oocytes. Interestingly, we found that instead of serine, the arginine residue in the SFRS motif was involved in pH sensing. Arginine is likely permanently positively charged, so R285A mutation shows that not only the length but the charge of distal CT is critical for pH gating. Through computational inspection on complete PIP models, we detected that possible conformations of CT distal part can interact with loopD, in particular with the pH sensor H202, and that the pKa of this sensor can be influenced by these interactions. Based on these data, we proposed that the last 6 residues of one monomeric *Bv*PIP2;2 CT can adopt positions of close spatial proximity with an adjacent monomeric loopD acting as an electrostatic shield on pH sensor residues of loopD. So, a quite acidic cytosolic pH is needed to close this channel.

We checked whether *Bv*PIP1;1 CT had a similar effect as that obtained with shorten *Bv*PIP2;2 CT on gating, by constructing the chimeric channel *Bv*PIP2;2CT1;1. The homotetrameric form of this chimeric protein was not functional when expressed alone. Other similar chimeric PIP2 have been reported previously. The activity reported for two of these constructs was almost null or lower in comparison with their corresponding wild-type PIP2 (chimeric *Nicotiana tabacum* PIP2;1 assayed in proteoliposomes— named P2_(C)A1— [27] and chimeric *Hordeum vulgare* PIP2;4_12NC expressed in *Xenopus laevis* oocytes [28]), and in the third case, water transport was not assayed (*Zea mays* PIP2;5Cter1;2 expressed in maize mesophyll protoplast [29]). We do not discard a specific regulation for these artificial channels depending on the sequence and expression system. Withal, in our case, the co-expression of *Bv*PIP2;2CT1;1 with *Bv*PIP1;1 or *Bv*PIP2;2 allowed inferring information about the chimeric channel showing that in this condition, it was fully functional. The interaction of

*Bv*PIP2;2CT1;1 with both *Bv*PIP1;1 and *Bv*PIP2;2 renders heterotetramers with a shifted $pH_{0.5}$ in comparison with *Bv*PIP2;2 homotetramers, but at a different extent. Interestingly, in *Bv*PIP2;2CT1;1-*Bv*PIP1;1 co-expression, where all CT are short, $pH_{0.5}$ is ~ 6.8, but in *Bv*PIP2;2CT1;1-*Bv*PIP2;2 co-expression, with a mixed population of long and short CT, $pH_{0.5}$ is ~6.6. This last result contrasts with the higher $pH_{0.5}$ value found for *Bv*PIP2;2-*Bv*PIP1;1 heterotetramers (~ 6.8) [11,30]. We suspect that, in heterotetramers, PIP1 NT plays a role on PIP2 long CT detaching from a neighboring loopD, a function that PIP2 NT cannot accomplish. The MDS and CpHMD results obtained for the 3 : 1 *Bv*PIP1;1-*Bv*PIP2;2 heterotetramer confirm that even when one long or "PIP2 type" CT can reach the adjacent monomeric loopD, interactions found in PIP2 homotetramers are lost and pH sensor pKa is similar to the obtained with short CT. This hypothesis about the putative PIP1 NT mechanism of action on heterotetramers gating deserves additional experiments and goes beyond the scope of this work.

In summary, the main output of the set of experiments presented here is that: (a) the open/closed transition in PIP tetramers occurs at a quite acidic pH (~ 6.4) only when all CT are long, or "PIP2 type", (b) if all CT are short, the open/closed transition occurs at alkaline pH values (~ 6.8), and (c) when mixed long and short CT are present in the tetramers, the open/closed transition presents a shift in $pH_{0.5}$ (~ 6.6 to ~ 6.8 depending on the kind of NT in the tetramer).

All homotetrameric PIP2 channels whose pH gating has been tested show a similar acidic $pH_{0.5}$ except for *At*PIP2;1 [4,11,22,31–33]. It is difficult to anticipate conclusions regarding this difference, but interestingly pH gating for this channel was assayed in proteoliposomes and not in a cellular context. The possibility of a calcium-binding site in PIP2 CT was proposed after finding Cd^{2+} ions in the crystal structure of *So*PIP2;1-Hg preparations, and it was suggested that this cation could play a role in the stabilization of closed conformation by connecting CT with loopD [5].

As mention before, phosphorylation of CT serines was shown to be involved in trafficking and regulation of water and ion transport [24,25,34]. And interestingly, interactome studies discovered that some PIP CT behaves as a platform for recruitment of a wide range of regulatory proteins both activating and inhibiting water transport [35,36]. All these reports in combination with our results point to a dual role of PIP CT in protein–protein interaction and gating. Regarding gating, while its presence is not necessary to guarantee the open/closed transition, the distal part of PIP2 C-terminal region modulates the channel pH

sensor and plays a direct role in defining the degree of cytosolic acidification at which PIP channels get closed. So, channel opening would occur under quite acidic pH values in most homotetrameric PIP2 channels, while PIP2-PIP1 heterotetramers or PIP2 homotetramers whose distal CT is compromised in interactions that interrupt pH sensor shielding will close at mildly acidic conditions. Future work would clarify how the multiple signals shown to impact in CT functionality operate in the different biological scenarios a plant cell can go through.

Materials and methods

Sequence retrieval, alignments, and generation of sequence LOGOs

Aquaporin protein sequences of *Bv*PIP2;2 and *Bv*PIP1;1 were used as query to search against plant genome databases including Phytozome (www.phytozome.net) and NCBI (www.ncbi.nlm.nih.gov) using BLASTP. Aquaporins from thirty-four different plants were considered (*Arabidopsis lyrate*, *Arabidopsis thaliana*, *Beta vulgaris*, *Brachypodium distachyon*, *Cenchrus americanus*, *Cucumis sativus*, *Fragaria vesca*, *Fragaria x ananassa*, *Glycine max*, *Hedychium coronarium*, *Hevea brasiliensis*, *Hordeum vulgare*, *Lotus japonicus*, *Malus domestica*, *Medicago truncatula*, *Musa acuminata*, *Nicotiana tabacum*, *Oryza sativa*, *Phaseolus vulgaris*, *Physcomitrella patens*, *Picea abies*, *Picea sitchensis*, *Populus trichocarpa*, *Prunus persica*, *Ricinus communis*, *Selaginella moellendorffii*, *Setaria itálica*, *Solanum tuberosum*, *Sorghum bicolor*, *Spinacia oleracea*, *Theobroma cacao*, *Triticum aestivum*, *Vitis vinifera*, *Zea mays*), and 111 sequences from PIP2 and 119 from PIP1 were included in the analysis. Seqkit was used to eliminate the repeated sequences [37]. For each group, protein sequences were aligned using Clustal implemented in Jalview [38]. The length of CT was determined based on the crystal structure of SoPIP2;1 (1Z98) and sequence alignment, taking the GLN270 as the first residue of the domain in *Bv*PIP2;2.

DNA constructions

*Bv*PIP2;2 and mutants were subcloned into pT7T-derived vector as detailed previously [11,22]. The chimeric protein *Bv*PIP2;2CT1;1 was created by two-step PCR. The *Bv*PIP1;1 CT that replaces *Bv*PIP2;2 CT was determined by sequence alignment, and residues following *Bv*PIP2;2 GLN270 were replaced by the corresponding *Bv*PIP1;1 CT residues. Truncation of the *Bv*PIP2;2 CT was performed by one-step PCR using primers overlapping the deleted sequence. Mutants encoding *Bv*PIP2;2R285A and *Bv*PIP2;2S283A were obtained by site-directed mutagenesis

Table 1. Primers used to construct *Bv*PIP mutants.

Primer name	Direction	Sequence (5′–3′)	DNA Construction
Fw *Bv*PIP2;2	Forward	GGGAGATCTATGACCAAGGATGTGGAAGCAGTTTC	*Bv*PIP2;2Δ6CT and *Bv*PIP2;2CT1;1
SpeI-*Bv*PIP2;2CT_R	Reverse	GGACTAGTTTATCCTAGAGCTTTGATTGCACCAGCTC	*Bv*PIP2;2Δ6CT
*Bv*PIP2;2CT1_A	Reverse	TGGAATTGCCCTGATCACCACTGTGTGGTAAAATGCTGCAATTGC	*Bv*PIP2;2CT1;1
*Bv*PIP2;2CT1_B	Reverse	GGACTAGTTTACGACTTGGACTTGAATGGAATTGCCCTGAT	*Bv*PIP2;2CT1;1
Fw_*Bv*PIP2;2R285A	Forward	GCTCTAGGATCCTTCGCTAGCTCTGCTTAA	*Bv*PIP2;2R285A
Rev_*Bv*PIP2;2R285A	Reverse	TTAAGCAGAGCTAGCGAAGGATCCTAGAGC	*Bv*PIP2;2R285A
Fw_*Bv*PIP2;2S283A	Forward	GCAATCAAAGCTCTAGGAGCCTTCAGGAGCTCTG	*Bv*PIP2;2S283A
Rev_*Bv*PIP2;2S283A	Reverse	CAGAGCTCCTGAAGGCTCCTAGAGCTTTGATTGC	*Bv*PIP2;2S283A

using custom-made oligonucleotide primers. The primers used are listed in Table 1. All the constructs were verified by DNA sequencing (Macrogen Inc., Seoul, Korea).

In vitro RNA synthesis, oocyte isolation, and cell injection

The capped complementary RNA (cRNA) encoding *Bv*PIP1;1, *Bv*PIP2;2, and mutants was synthesized *in vitro* using the mMESSAGEmMACHINE T7 High Yield Capped RNA Transcription Kit (Ambion, Austin, Texas, USA) or with mMESSAGEmMACHINE T7 High Yield Capped RNA ULTRA Transcription Kit (Ambion, Austin, Texas, USA). Agarose gel electrophoresis and Gel Red (BioAmerica Biotech Inc., Miami, Florida, USA) staining were used to check the absence of unincorporated nucleotides in the cRNA in each *in vitro* cRNA synthesis. The synthesized products were quantified using BioTek's Gen5TM microplate reader (BioTek, Winooski, Vermont, USA). The cRNA was suspended in RNAse-free water and stored at −20 °C until use. At least two independent cRNA syntheses were assayed. *Xenopus laevis* (Nasco, Fort Atkinson, Wisconsin, USA) defolliculated oocytes (stage V–VI) were used for expression of different PIP channels. Isolation and maintenance of oocytes were carried out as previously described [11,32]. Each oocyte was microinjected (Drummond Scientific Co, Broomall, Pennsylvania, USA) with 50 nL of a solution containing a proper amount of cRNA (5-15 ng). All injected oocytes were kept during 72 h at 18 °C in ND96 buffer solution (96 mM NaCl, 2 mM KCl, 1 mM MgCl₂, 1.8 mM CaCl₂, and 5 mM HEPES pH 7.5; ~ 200 mOsmol·kg⁻¹ H₂O) supplemented with 1 g·L⁻¹ gentamicin (GIBCO, Waltham, Maryland, USA) at 18 °C before performing the experiments.

Water transport assays and pH dose–response experiments

The osmotic water permeability (P_f) of oocytes injected or noninjected with cRNA was determined by measuring the rate of oocyte swelling as previously described [11,32]. P_f was calculated according to Zhang & Verkman [39]. For

pH inhibition experiments, the oocyte internal (cytosolic) pH was modified following a protocol optimized previously [4]. Briefly, the internal pH of oocytes was acidified by pre-incubating them for 20 min in different acetate solutions (50 mM sodium acetate, 20 mM MES for the 5.8–6.8 pH interval, or HEPES for the 7.0–7.4 pH interval), supplemented with mannitol 1 M until the desired osmolarity was achieved (~ 200 mOsmol·kg⁻¹ H₂O). The internal pH was then calculated following the calibration performed in Bellati *et al.* [22]. Briefly, BCECF B-1151 (Molecular Probes, Eugene, Oregon, USA) was injected into oocytes (100 μM). Fluorescence ratio (490/440 nm) was acquired with a Nikon TE-200 Epifluorescence Inverted Microscope. Calibration curve was generated by incubating oocytes with different sodium acetate pH solutions. The swelling response was induced by transferring the oocytes to a 5-fold dilution of the solution of incubation. Relative P_f was obtained by the equation:

$$Relative\,P_f = \frac{\left(P_f - mean\,P_{f\,pH6.3}\right)}{mean\,P_{f\,pH7.2} - mean\,P_{f\,pH6.3}} \times 100$$

Relative P_f values are used to discard any possible difference in the translating rate or membrane insertion rate among the mutant and the wild-type channels that can cause functional data to be misinterpreted. For pH dose–response curves, the empirical sigmoidal function was used:

$$Relative\,P_f = P_{fmin} + \frac{\left(P_{fmax} - P_{fmin}\right)}{\left(1 + 10^{(pH_{0.5} - pH_{int})nH}\right)}$$

Relative P_f was fitted to experimental data by nonlinear regression, where P_{fmax} and P_{fmin} are the asymptotic maximal and minimal values of relative P_f, pH is the experimental internal oocyte pH, $pH_{0.5}$ is pH at with the water permeability change is half-maximal, and nH is an empirical coefficient representing the curve sigmoidicity. Noninjected oocytes were used as negative controls because no significant differences were found between this condition and water-injected oocytes. All dose–response curves shown in figures are representative of at least three different experiments (i.e., results from experiments performed with different oocyte

batches were not pooled). The osmolarities of all solutions used were determined using a Vapor Pressure Osmometer (5600C Wescor Inc., Logan, Utah, USA).

Computational methods

Model construction

The *Bv*PIP2;2 model was built in several steps from *So*PIP2;1 closed conformation crystallographic structure (PDB 1Z98). Initially, the last 7 residues of *So*PIP2;1 (distal CT) were modeled by comparative and homology modeling using Modeller [40] on a preheated structure. This step produced a tetramer with 4 unique distal CT conformations, one for each monomer. Secondly, the very first 34 residues of *So*PIP2;1 (NT) were modeled on Robetta web server [41], isolated from the rest of the protein. This step produced 5 models from which we picked the 4 with the best scores. These 4 models were thermalized independently and ran in a MD simulation performed in explicit solvent (TIP3P water) and ions (NaCl 0.15 м) for 5 ns. These models were carefully done including 11 residues already present in the full structure in order to ease the following step. Thirdly, the NT models were attached to the tetramer obtained in the first step, which already had a full-length CT. The NT attachments were carried out by fitting those 11 residues present in both NT and tetramer models. Finally, *Bv*PIP2;2 model was obtained by homology modeling using the full-length *So*PIP2;1 as a template in the Swiss Model web server [42]. This model was embedded in a fully hydrated 124 × 124 Å POPC bilayer using the membrane builder tool provided in the CHARMM-GUI web server[43]. *Bv*PIP2;2Δ6CT was built from the full-length *Bv*PIP2;2 model by deleting the last 6 residues from each monomer. *Bv*PIP2;2-*Bv*PIP1;1 heterotetramer was built by, firstly, obtaining an *Bv*PIP1;1 homotetramer through homology modeling with Swiss Model, using the herein obtained *Bv*PIP2;2 model as a template. The first 2 and the last 2 residues from each monomer were added with PyMol, using the Build tool, as Swiss Model was not able to model those residues. Finally, *Bv*PIP1;1 and *Bv*PIP2;2 homotetramers were aligned in PyMol and the desired monomers were deleted to obtain a 3:1 heterotetramer. This model was then embedded in a POPC bilayer as described above. Every model render was obtained with VMD software [44].

Plain molecular dynamics simulations

Four replicate simulation runs of 100 ns each were carried out for all systems (*Bv*PIP2;2, *Bv*PIP2;2-H+, *Bv*PIP2;2Δ6CT, and *Bv*PIP1;1-*Bv*PIP2;2 heterotetramer). Initial coordinates for each replica were taken from evenly distributed snapshots of an independent 80-ns simulation. For *Bv*PIP2;2 and *Bv*PIP2;2-H+ simulations, the same set of initial snapshots was used. All plain molecular dynamics simulations were performed as described previously in Canessa Fortuna *et al.* [18]. Briefly, systems were minimized prior to heating stages. Heating was carried out under weak harmonic constraints from 0K to 303K. Thereafter, constrain-free molecular dynamics simulations were run in an NPT ensemble with full periodic boundary conditions. Nonbonded interactions were simulated with a cutoff of 10 Å. Particle Mesh Ewald was used for long range electrostatic interactions. All simulations were performed with AMBER18 MD package [45] and parameters from AMBER14SB and LIPID17 force fields [46,47]. Trajectory analysis involving contacts, SASA, RDF, and RMSD was carried out in CPPTRAJ trajectory analysis tool from the AmberTools package. The solvent-accessible surface area (SASA) calculations were computed using linear combination of pairwise overlaps (LCPO) algorithm. MDLovofit [48] fit was performed prior to RMSD analysis. For those analyses, the last 19, 13, and 13 residues were considered as CT for *Bv*PIP2;2, *Bv*PIP2;2Δ6CT and *Bv*PIP1;1, respectively. Contact relative frequency was calculated as it provides information about the probability of a certain interaction. This was computed as the total contacts along the simulated trajectory divided by the total number of frames. A certain contact in a simulation frame was computed if the shortest distance between the aforementioned residues was less than 5 Å. Only contacts shorter than 5 Å were considered for analysis. For RDF analysis, atoms from every CT were taken into account to compute atom presence probability density as a function of radial distance to each H202 (or H205) in the tetramer.

Constant pH simulations and titration curves

Continuous constant pH molecular dynamics simulations (CpHMD) were performed to assess the pKa of the pH sensor, that is, H202 in both *Bv*PIP2;2 and *Bv*PIP2Δ6CT. This sampling method allows to change the protonation state of an amino acid along a molecular dynamics simulation. The protocol was adapted from Socher & Sticht [49]. Briefly, the proteins are simulated at constant pH, then solvent pH is increased, and a new simulation is restarted at the new pH, using coordinates and velocities from the previous simulation as an input. In each simulation, protonation state change is attempted every 50 steps using Monte Carlo sampling of the Boltzmann distribution of protonation states as implemented in the AMBER package. Deprotonated fraction (f_d) at each pH is then calculated from the outcome of each Monte Carlo step, and pKa was calculated as a fit parameter of the following Hill equation:

$$f_d(pH) = \frac{1}{1 + 10^{n(pKa - pH)}}$$

We used 0.25 pH units increments and 1-ns simulations for extreme pH and 0.1 pH units increments and 5-ns

simulations for the transition pH, for the sake of a better sampling in the transition.

Statistics

Results are reported as means ± SEM. Significant differences between groups were calculated, according to need, using a two-tailed Student's *t*-test or one-way ANOVA followed by Dunnet multiple comparison test with GRAPHPAD Prism 6.

Acknowledgments

Conflict of interest

The authors declare no conflict of interest.

Authors contribution

KA and AZ designed research and conceived the study. FS, GZP, ACF, GS, and AZ planned experiments. FS, GZP, and JC performed experiments. FS, GZP, ACF, JC, KA, and AZ analyzed data. GS and RT contributed reagents and essential materials for the investigation. FS, ACF, and GZP produced figures. KA and AZ supervised research. KA wrote the paper with critical feedback from all authors.

Peer review

The peer review history for this article is available at https://publons.com/publon/10.1111/febs.16134.

References

1 Verdoucq L & Maurel C (2018) Chapter Two - Plant aquaporins. In Advances in Botanical Research (Maurel C, ed.), 1st edn, Vol. 87, pp. 25–56. Academic Press. https://www.sciencedirect.com/science/article/pii/S0065229618300557

2 Chaumont F & Tyerman SD (2014) Aquaporins: highly regulated channels controlling plant water relations. *Plant Physiol* **164**, 1600–1618.

3 Jozefkowicz C, Berny MC, Chaumont F & Alleva K (2017) Heteromerization of plant aquaporins. In Signaling and Communication in Plants (Chaumont F & Tyerman S, eds), pp. 29–46. Springer, Cham. https://doi.org/10.1007/978-3-319-49395-4_2

4 Tournaire-Roux C, Sutka M, Javot H, Gout E, Gerbeau P, Luu DTD-T, Bligny R & Maurel C (2003) Cytosolic pH regulates root water transport during anoxic stress through gating of aquaporins. *Nature* **425**, 393–397.

5 Frick A, Järvå M & Törnroth-Horsefiel S (2013) Structural basis for pH gating of plant aquaporins. *FEBS Lett* **587**, 989–993.

6 Törnroth-Horsefield S, Wang Y, Hedfalk K, Johanson U, Karlsson M, Tajkhorshid E, Neutze R & Kjellbom P (2006) Structural mechanism of plant aquaporin gating. *Nature* **439**, 688–694.

7 Bienert MD, Diehn TA, Richet N, Chaumont F & Bienert GP (2018) Heterotetramerization of Plant PIP1 and PIP2 aquaporins is an evolutionary ancient feature to guide PIP1 plasma membrane localization and function. *Front Plant Sci* **9**, 1–15.

8 Anderberg HI, Kjellbom P & Johanson U (2012) Annotation of Selaginella moellendorffii Major Intrinsic Proteins and the Evolution of the Protein Family in Terrestrial Plants. *Front Plant Sci* **3**, 33.

9 Soto G, Alleva K, Amodeo G, Muschietti J & Ayub ND (2012) New insight into the evolution of aquaporins from flowering plants and vertebrates: Orthologous identification and functional transfer is possible. *Gene* **503**, 165–176.

10 Yaneff A, Sigaut L, Marquez M, Alleva K, Pietrasanta LI & Amodeo G (2014) Heteromerization of PIP aquaporins affects their intrinsic permeability. *Proc Natl Acad Sci* **111**, 231–236.

11 Jozefkowicz C, Sigaut L, Scochera F, Soto G, Ayub N, Pietrasanta LI, Amodeo G, González Flecha FL & Alleva K (2016) PIP water transport and its pH dependence are regulated by tetramer stoichiometry. *Biophys J* **110**, 1312–1321.

12 Berny MC, Gilis D, Rooman M & Chaumont F (2016) Single mutations in the transmembrane domains of maize plasma membrane aquaporins affect the activity of monomers within a heterotetramer. *Mol Plant* **9**, 986–1003.

13 Fetter K, Van Wilder V, Moshelion M & Chaumont F (2004) Interactions between plasma membrane aquaporins modulate their water channel activity. *Plant Cell* **16**, 215–228.

14 Otto B, Uehlein N, Sdorra S, Fischer M, Ayaz M, Belastegui-Macadam X, Heckwolf M, Lachnit M, Pede N, Priem N *et al.* (2010) Aquaporin tetramer

composition modifies the function of tobacco aquaporins. *J Biol Chem* **285**, 31253–31260.

15 Bienert GP, Cavez D, Besserer A, Berny MC, Gilis D, Rooman M & Chaumont F (2012) A conserved cysteine residue is involved in disulfide bond formation between plant plasma membrane aquaporin monomers. *Biochem J* **445**, 101–111.

16 Gerbeau P, Amodeo G, Henzler T, Santoni V, Ripoche P & Maurel C (2002) The water permeability of Arabidopsis plasma membrane is regulated by divalent cations and pH. *Plant J* **30**, 71–81.

17 Alleva K, Niemietz CM, Sutka M, Maurel C, Parisi M, Tyerman SD & Amodeo G (2006) Plasma membrane of Beta vulgaris storage root shows high water channel activity regulated by cytoplasmic pH and a dual range of calcium concentrations. *J Exp Bot* **57**, 609–621.

18 Canessa Fortuna A, Zerbetto De Palma G, Aliperti Car L, Armentia L, Vitali V, Zeida A, Estrin DA & Alleva K (2019) Gating in plant plasma membrane aquaporins: the involvement of leucine in the formation of a pore constriction in the closed state. *FEBS J* **286**, 3473–3487.

19 Nyblom M, Frick A, Wang Y, Ekvall M, Hallgren K, Hedfalk K, Neutze R, Tajkhorshid E & Törnroth-Horsefield S (2009) Structural and functional analysis of SoPIP2;1 mutants adds insight into plant aquaporin gating. *J Mol Biol* **387**, 653–668.

20 Fischer M & Kaldenhoff R (2008) On the pH regulation of plant aquaporins. *J Biol Chem* **283**, 33889–33892. https://doi.org/10.1074/jbc.m803865200

21 Wang H, Schoebel S, Schmitz F, Dong H & Hedfalk K (2020) Characterization of aquaporin-driven hydrogen peroxide transport. *BBA - Biomembr* **1862**, 183065.

22 Bellati J, Alleva K, Soto G, Vitali V, Jozefkowicz C & Amodeo G (2010) Intracellular pH sensing is altered by plasma membrane PIP aquaporin co-expression. *Plant Mol Biol* **74**, 105–118.

23 Vitali V, Jozefkowicz C, Canessa Fortuna A, Soto G, González Flecha FL & Alleva K (2019) Cooperativity in proton sensing by PIP aquaporins. *FEBS J* **286**, 991–1002.

24 Prak S, Hem S, Boudet J, Viennois G, Sommerer N, Rossignol M, Maurel C & Santoni V (2008) Multiple phosphorylations in the C-terminal tail of plant plasma membrane aquaporins. *Mol Cell Proteomics* **7**, 1019–1030. https://doi.org/10.1074/mcp.m700566-mcp200

25 Tyerman SD, McGaughey SA, Qiu J, Yool AJ & Byrt CS (2021) Adaptable and multifunctional ion-conducting aquaporins. *Annu Rev Plant Biol* **72**, 1–34.

26 Qiu J, McGaughey SA, Groszmann M, Tyerman SD & Byrt CS (2020) Phosphorylation influences water and ion channel function of AtPIP2;1. *Plant Cell Environ* **43**, 2428–2442.

27 Glitsos G (2017) N- and C-terminal domains in tobacco aquaporins –Analysis of protein-mediated water permeability in vitro and in silico. Darmstadt, Technische Universität Darmstadt, [Ph.D. Thesis]. https://tuprints.ulb.tu-darmstadt.de/id/eprint/6124

28 Shibasaka M, Horie T & Katsuhara M (2021) Mechanisms activating latent functions of PIP aquaporin water channels via the interaction between PIP1 and PIP2 proteins. *Plant Cell Physiol* **62**, 92–99. https://doi.org/10.1093/pcp/pcaa142

29 Zelazny E, Miecielica U, Borst JW, Hemminga MA & Chaumont F (2009) An N-terminal diacidic motif is required for the trafficking of maize aquaporins ZmPIP2;4 and ZmPIP2;5 to the plasma membrane. *Plant J* **57**, 346–355.

30 Jozefkowicz C, Scochera F & Alleva K (2016) Two aquaporins, multiple ways of assembly. *Channels* **10**, 438–439.

31 Verdoucq L, Grondin A & Maurel C (2008) Structure–function analysis of plant aquaporin AtPIP2; 1 gating by divalent cations and protons. *Biochem J* **415**, 409–416.

32 Jozefkowicz C, Rosi P, Sigaut L, Soto G, Pietrasanta LI, Amodeo G & Alleva K (2013) Loop a is critical for the functional interaction of two beta vulgaris PIP aquaporins. *PLoS One* **8**, e57993.

33 Fox AR, Scochera F, Laloux T, Filik K, Degand H, Morsomme P, Alleva K & Chaumont F (2020) Plasma membrane aquaporins interact with the endoplasmic reticulum resident VAP27 proteins at ER–PM contact sites and endocytic structures. *New Phytol* **228**, 973–988.

34 Johansson I, Karlsson M, Shukla VK, Chrispeels MJ, Larsson C & Kjellbom P (1998) Water transport activity of the plasma membrane aquaporin PM28A is regulated by phosphorylation. *Plant Cell* **10**, 451–459.

35 Bellati J, Champeyroux C, Hem S, Rofidal V, Krouk G, Maurel C & Santoni V (2016) Novel aquaporin regulatory mechanisms revealed by interactomics. *Mol Cell Proteomics* **15**, 3473–3487.

36 Prado K, Cotelle V, Li G, Bellati J, Tang N, Tournaire-Roux C, Martinière A, Santoni V & Maurela C (2019) Oscillating aquaporin phosphorylation and 14-3-3 proteins mediate the circadian regulation of leaf hydraulics. *Plant Cell* **31**, 417–429.

37 Shen W, Le S, Li Y & Hu F (2016) SeqKit: A cross-platform and ultrafast toolkit for FASTA/Q file manipulation. *PLoS One* **11**, 1–10.

38 Waterhouse AM, Procter JB, Martin DMA, Clamp M & Barton GJ (2009) Jalview Version 2-A multiple sequence alignment editor and analysis workbench. *Bioinformatics* **25**, 1189–1191. https://doi.org/10.1093/bioinformatics/btp033

39 Zhang R & Verkman AS (1991) Water and urea permeability properties of Xenopus oocytes: expression of mRNA from toad urinary bladder. *Am J Physiol Cell Physiol* **260**, C26–C34.

40 Webb B & Sali A (2016) Comparative protein structure modeling using MODELLER. *Curr Protoc Bioinforma* **54**, 5.6.1-5.6.37.

41 Song Y, Dimaio F, Wang RYR, Kim D, Miles C, Brunette T, Thompson J & Baker D (2013) High-resolution comparative modeling with RosettaCM. *Structure* **21**, 1735–1742.

42 Waterhouse A, Bertoni M, Bienert S, Studer G, Tauriello G, Gumienny R, Heer FT, de Beer TAP, Rempfer C, Bordoli L *et al.* (2018) SWISS-MODEL: homology modelling of protein structures and complexes. *Nucleic Acids Res* **46**, W296–W303. https://doi.org/10.1093/nar/gky427

43 Jo S, Kim T, Iyer WG & Im W (2008) CHARMM-GUI: a web-based graphical user interface for CHARMM. *J Comput Chem* **29**, 1859–1865.

44 Humphrey W, Dalke A & Schulten K (1996) VMD: visual molecular dynamics. *J Mol Graph* **14**, 33–38.

45 Case D, Ben-Shalom IY, Brozell SR, Cerutti DS, Cheatham TEI, Cruzeiro VW, Darden TA, Duke RE, Ghoreishi D, Gilson MK *et al.* (2018) AMBER 18. University of California, San Francisco.

46 Maier JA, Martinez C, Kasavajhala K, Wickstrom L, Hauser KE & Simmerling C (2015) ff14SB : improving the accuracy of protein side chain and backbone parameters from ff99SB. *J Chem Theory Comput* **11**, 3696–3713. https://doi.org/10.1021/acs.jctc.5b00255

47 Dickson CJ, Madej BD, Skjevik ÅA, Betz RM, Teigen K, Gould IR & Walker RC (2014) Lipid14: the amber lipid force field. *J Chemital Theory Comput* **10**, 865–879.

48 Martínez L (2015) Automatic identification of mobile and rigid substructures in molecular dynamics simulations and fractional structural fluctuation analysis. *PLoS One* **10**, 1–10.

49 Socher E & Sticht H (2016) Mimicking titration experiments with MD simulations: a protocol for the investigation of pH-dependent effects on proteins. *Sci Rep* **6**, 1–13.